

# Influence of winding and shaft cooling on the thermal characteristics of a traction machine for heavy-duty distribution transport

BENEDIKT GROSCHUP  , DANIEL BUTTERWECK, KAY HAMEYER

*Institute of Electrical Machines (IEM), RWTH Aachen University*

*Schinkelstraße 4, 52062 Aachen, Germany*

*e-mail:  [benedikt.groschup@rwth-aachen.de](mailto:benedikt.groschup@rwth-aachen.de)*

(Received: 21.04.2023, revised: 19.06.2023)

**Abstract:** This paper studies the influence of different cooling technologies on the power density of a traction machine for heavy-duty distribution transport. A prototype induction machine is built with a housing cooling jacket, potted end-windings, entire winding cooling, and shaft cooling. Electromagnetic finite element and thermal lumped-parameter models are parameterized and verified using test bench measurements. The influence of each thermal resistance along the heat paths is studied and discussed. The results are used for studying different cooling technologies. The results indicate an improvement of the continuous power density up to 108% using shaft cooling and up to 15.6% using entire winding cooling.

**Key words:** cooling, thermal design, winding cooling

## 1. Introduction

Electric traction machines for heavy-duty commercial vehicles require high operational power under continuous operation, i.e., S1 according to IEC 60034-1 [1]. High power density designs desire innovative cooling technologies as discussed in [2]. The powertrain studied here consists of two electrical machines and a transmission as introduced in [3]. The key parameters of the induction machine that is focused in this study are depicted in Table 1. The machine is designed for a maximum rotational speed of  $n_{\max} = 10\,000$  rpm and a continuous power of  $P_{S1} = 203$  kW. This power can be achieved if all three cooling circuits are in operation. A cross-sectional view of the machine is given in Fig. 1. The housing cooling is realized with a tangential helix.

The stator winding cooling is designed with axial cooling pipes within the slot. The cooling pipes have a round shape. The pipe is bended in a S-shape on one side of the end-winding area. This



© 2023. The Author(s). This is an open-access article distributed under the terms of the Creative Commons Attribution-NonCommercial-NoDerivatives License (CC BY-NC-ND 4.0, <https://creativecommons.org/licenses/by-nc-nd/4.0/>), which permits use, distribution, and reproduction in any medium, provided that the Article is properly cited, the use is non-commercial, and no modifications or adaptations are made.

Table 1. Machine parameters

Specification	Variable	Value	Unit
Maximum rotational speed	$n_{\max}$	10 000	1 rpm
Pole pairs	$p$	3	
Cooling medium	–	EWG 50/50	
Volume flow of coolant	$\dot{V}_{\text{tot}}$	16	L/min
Housing diameter	$d_{\text{ho}}$	400	mm
Housing length	$l_{\text{ho}}$	480	mm
S1 power at 5 190 rpm	$P_{S1}$	203	kW

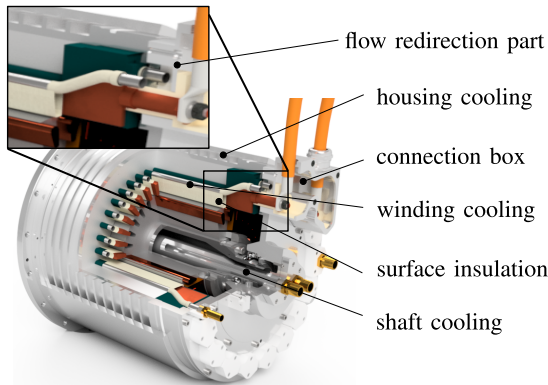


Fig. 1. Cross-sectional view of the studied induction machine

procedure enables sufficient installation space for the end-winding without collision with the rotor during assembly. Flow redirection parts are milled out of polyoxymethylene. The non-conductive material is selected to avoid eddy currents over the housing between the different cooling ducts. The shaft cooling has a one-sided in- and outlet with a stationary cooling lance inside the rotor. The three different cooling circuits are all designed with a volume flow of  $\dot{V}_{\text{tot}} = 16 \text{ L/min}$  and can be connected in serial. The total volume flow is split in two parallel channels for the winding cooling with  $\dot{V}_{\text{ch}} = 8 \text{ L/min}$  for each channel. A mixture of ethylene-glycole and water (EGW 50/50) is used for all cooling channels. A prototype of the machine is built to study the influence of the three cooling technologies. Measurements of the efficiency and the thermal heat paths in the machine are performed to gain well parameterized simulation models.

Special focus is given on the design and thermal heat path study of a winding cooling with water-based cooling fluid. The placement of the cooling circuit in the stator slot can be found in literature using oil-based cooling fluids [4, 5]. The advantage of such an oil-based design are the good chemical compatibility of the cooling fluid and the machine components.

The usage of water-based coolant in a slot leads to risks due to the low electric resistivity of the fluid and is rare. The approach to use de-ionized water seems to be non-practical in a real environment [6]. Oil-based cooling fluid can be directly applied to the winding but comes

with disadvantages regarding the fluid heating and the convective heat transfer of the thermal problem. A water-based coolant has high cooling potential but needs to be placed outside the surface insulation in the slot to avoid insulation issues. The potential of such a design highly depends on the local thermal resistances in the machine. A study of such local heat paths in the slot of a water-based winding cooling is rare.

Thermal finite element (FE) models are developed to study the local thermal interfaces in the slot of the studied machine. They are used to parameterize lumped parameter thermal network (LPTN) models that represent the characteristics of the machine. All models are parameterized using heat path measurements of the machine on a test bench. The resulting thermal models are used for a detailed study of the heat paths of the introduced winding cooling technology as well as a simulation study where different cooling technologies are considered. This comparison includes slight adaptations to the real prototype in order to guarantee a fair comparison of the cooling methodologies.

## 2. Prototype of the winding cooling

The studied induction machine has 36 stator slots. A cooling duct is placed in the outer part of each stator slot as shown in Fig. 2.

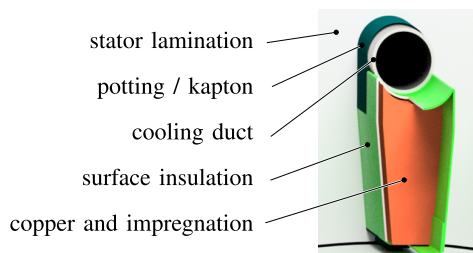


Fig. 2. Cross-sectional view of the stator slot

The cooling ducts are manufactured of stainless steel to ensure high thermal conductivity. A thin Kapton layer is placed between each cooling duct and the stator lamination to avoid eddy currents. The cooling ducts are placed outside the surface insulation, i.e., the ducts do not have direct contact with the conductors of the stator winding. The path of a short circuit or partial discharge between the different phases of the machine needs to go over the surface insulation, i.e., a short circuit over the cooling duct is not possible. The cooling ducts are pre-bent in a S-shape to ensure sufficient installation space of the end-winding on the side of the wiring. The end-winding is not allowed to radially intrude into the stator bore to enable axial inserting the rotor into the stator. The cooling duct is straight on the non-wiring side, because it needs to be axially inserted into the stator lamination. The end-winding on this side radially intrudes into the stator bore. The round design of the cooling duct cross-sectional area is used due to its good availability in the first functional prototype. More advanced cross-sectional shapes could be possible in a later design step.

To ensure high copper fill factor and a proper placement of the surface insulation in the slot, the surface insulation and the pre-bent pipes are glued before inserting into the stator lamination.

The adhesive Elantas EP201 is used. The surface insulation material is a vonRoll Acuflex AHA HTC 232 with a thermal conductivity of 0.23 W/(m K). A thin Kapton layer as depicted in Fig. 2 with 0.06 mm is inserted into the slot to avoid eddy currents between the cooling ducts. The round-wire winding with a copper diameter of 1.12 mm and a peek-insulation with 75  $\mu$ m is assembled in a manual winding process. The entire winding is potted in a vacuum potting process using Von Roll DOLPHON C(a)-1123 resin with a RE-2023 hardener. The cured impregnation has a thermal conductivity of 1.27 W/(m K). The machine is equipped with thermocouples type J in 23 locations. Seven of the locations are placed in the rotor of the machine.

### 3. Thermal simulation models

The used three dimensional lumped-parameter thermal network models (LPTN) are based on a similar approach as introduced in [7, 8]. The axial length of the machine is modeled in three slices. A comparison of the machine geometry and the nodes of the 3D-LPTN is depicted in Fig. 3. The stator winding is modeled by two cuboidal elements in radial direction per axial slice [9]. One cuboidal element in the rotor per axial slice proved to be sufficient due to the solid rotor bar. The thermal conductivity of the soft magnetic material is determined by an indirect measurement approach of the thermal diffusivity as described in [10]. The convective heat transfer in stator and housing cooling is calculated using flow-dependent dimensionless correlations [11]. The thermal resistance from the fluid in the winding cooling to the three surrounding elements in the stator is calculated based on area-based weighting. The stator teeth are radially subdivided in four elements. One element represents the surface of the stator teeth in the air gap, two middle stator tooth elements are placed on a similar diameter as the cuboidal elements in the stator winding, and one element is placed between the stator yoke and the outer part of the teeth.

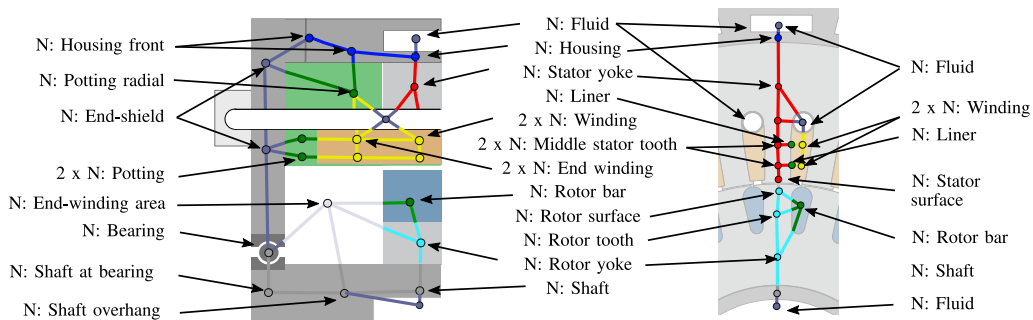


Fig. 3. Comparison of machine geometry and nodes of the 3D-LPTN model

The end-winding is fully potted. Two nodes are inserted to axially connect the cuboidal elements in the end-winding with the nodes of the end-shield. One radially inserted potting node is inserted for connecting housing and end-shield with the winding. The end-winding area heat transfer coefficient  $h$  is modeled by an analytical formula according to the formulation of Di Gerlando [7]. One axial slice of this 3D-LPTN model is selected for the 2D-LPTN, i.e., the

axial sectional-view that is depicted in Fig. 3. This model is used as a link between 3D-LPTN and 2D-FE model. The 2D-FE model has a high geometrical resolution and is used to parameterize the resistances of the cuboidal elements. It is further used for the study of the local heat paths.

Seven different variations of the thermal model are developed to study the influence of cooling methodologies on power density. The introduced nomenclature to describe the models is shown in Table 2.

Table 2. Nomenclature of simulation models

Digit	Variable	1	2	3	4
1	primary stator cooling	no cooling	housing without potting	housing with potting	entire winding
2	secondary stator cooling	no cooling	housing without potting	housing with potting	entire winding
3	type of rotor cooling	no cooling	rotor shaft		

It consists of three digits. The first digit describes the primary stator cooling, the second digit describes the secondary stator cooling, and the last digit describes the utilized rotor cooling technology. A comparison of the geometry and the most relevant thermal nodes is given in Fig. 4.

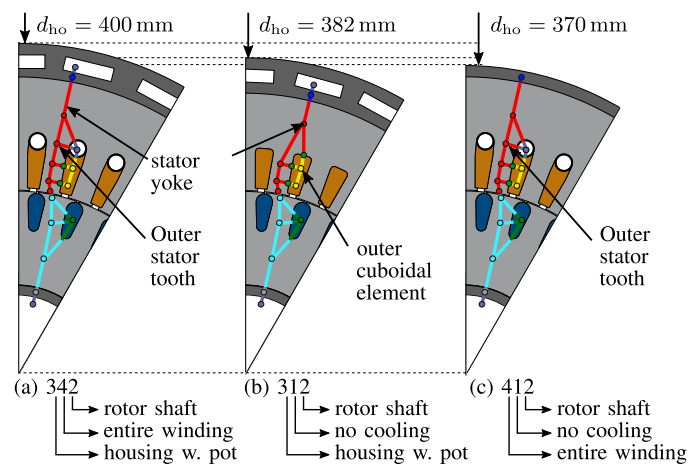


Fig. 4. Differences between the considered geometries and thermal models

Model 342 represents the built prototype with a housing cooling with potting, an entire winding cooling, and a rotor shaft cooling. The prototype is designed as a technology carrier, i.e., the housing cooling and the winding cooling are not designed to complement each other but fulfill the similar function. Model 312 represents a design with stator housing and rotor shaft cooling. The outer stator tooth node and the fluid node of the entire winding cooling is removed in this model.

The thickness of the stator yoke is kept constant in comparison to model 342. The designed adjustment leads to a reduction of the outer diameter from  $d_{ho} = 400$  mm (model 342) to a value of  $d_{ho} = 382$  mm (model 312). The area of the stator slot remains constant, and therefore, constant stator current-heat losses are assumed. The part of the iron losses in the outer stator tooth are not considered in this case. A similar procedure is performed to derive model 412 with winding cooling and shaft cooling. In this case, the outer part of the housing that is designed for sealing the housing cooling channel is removed. The outer diameter is assumed to be  $d_{ho} = 370$  mm in this case. Losses caused by the dynamic shaft sealing that are identified in a drag loss measurement are neglected in models without shaft cooling.

#### 4. Electromagnetic simulation model

The used electromagnetic simulation approach is based on a two-dimensional hybrid finite element model as introduced in [12]. The cross-sectional view of model 342 is used for the electromagnetic simulation. The losses are identified separately for the stator yoke and for four different radial sections of the stator tooth, i.e., the stator tooth tip, two radial sections with the size of the cuboidal elements in the winding, and one section with the size of the cooling duct. The losses in the last section of the stator tooth are not added to the thermal simulation of model 312 because the tooth is shortened in this model. A time-based calculation approach of the iron losses is necessary due to the significant differences between simulation and sampling frequencies of the transient model [12]. The available Bertotti formula is expanded by a non-linear loss term [13]. A general expression of this IEM 5-parameter formula be given [14]:

$$P_{fe} = a_1 \hat{B}^{\alpha+\hat{B}\beta} f + a_2 \hat{B}^2 f^2 + a_3 a_4 \hat{B}^{2+a_4} f^2 + a_5 \hat{B}^{1.5} f^{1.5}, \quad (1)$$

with the iron loss coefficients  $a_1, \dots, a_5$ ,  $\alpha$ ,  $\beta$ , the amplitude of the magnetic flux density  $\hat{B}$ , and the frequency  $f$ .

The first term describes hysteresis losses, the second term represents eddy current losses, the third term represents non-linear losses, and the last term is a representation of excess losses. The iron loss parameters are identified in a semi-physical approach based on single sheet measurements [15]. The rotor current heat losses are calculated using local eddy currents of the transient finite element simulation [12]. The influence of the local rotor current harmonics that are caused by the interaction between stator and rotor slots are negligible in [12], whereas the harmonics in the studied machine are significant, i.e., the influence of the rotational speed on the rotor current heat losses cannot be neglected, and simulating rotor current heat losses with a reference frame of stator current and rotor frequency and successive machine scaling cannot be used. A calculation based on an electromagnetic two-dimensional simulation with a simulation grid in the torque-speed reference frame is necessary. Skin and proximity effects of the round-wire winding in the stator are considered in the calculation of the stator current heat losses. The analytical model described in [16] is used. The influences of the inverter switching are included utilizing a fundamental wave model of the induction machine as introduced in [12].

### 5. Test bench setup

The built prototype is measured on a test bench as shown in Fig. 5.

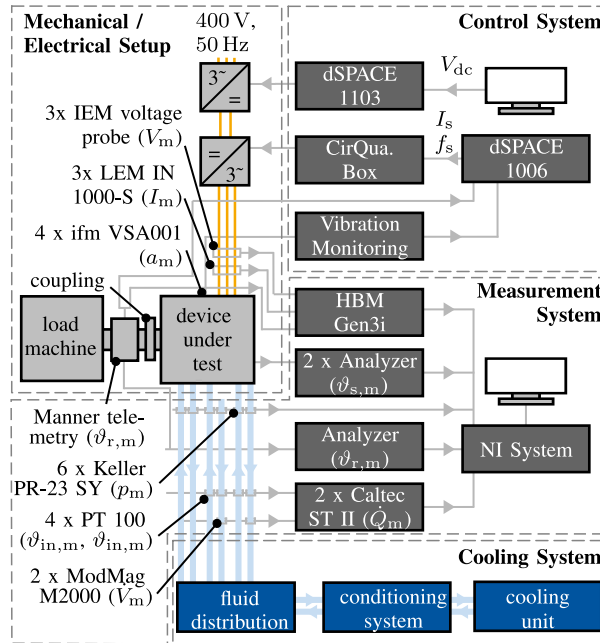


Fig. 5. Schematic overview of the test bench

The device under test (DUT) is mechanically connected to a load machine via a coupling, an HBM-T12 torque and speed transducer, and a Manner telemetry system for rotor temperature measurement. The control system of the test bench consists of a central monitoring system implemented on a dSPACE 1006. The DUT is controlled by a Cirqua.Box. A dSPACE 1103 system is used for controlling the battery simulator that provides the dc-link for the test bench. The measurement quantities are analyzed by an NI-measurement system. The electrical power measurement of the device under test is performed by an HBM GEN GN610B power analyzer that gets measurement signals from three IEM voltage probes and three LEM IN 1000-S current transducers. The temperatures are measured at 23 different locations using thermocouples. Seven thermocouples are placed in the rotor of the machine and transmitted by the telemetry system. The other temperature sensors are placed in the stator of the prototype and are transmitted by two IEM temperature analyzers. The cooling system consists of a Single STW130 conditioning system and a Huber Unichiller 080T cooling unit. All three cooling circuits can be switched on and off using a fluid distribution board. Caloric heat measurements  $\dot{Q}$  of the shaft and the winding cooling circuit are performed by two Caltec ST II heat flow analyzers. An indirect measurement technique for the heat flow  $\dot{Q}$  is used.

$$\dot{Q} = \rho c_p \dot{V} \Delta \vartheta, \tag{2}$$

with the density of the cooling fluid  $\rho$  and the specific heat capacity of the cooling fluid  $c_p$  that are both extracted from the data sheets of the used EGW 50/50. The necessary measurement of the volume flow  $\dot{V}$  is performed by two electromagnetic inductive flowmeters ModMag M2000, and the necessary temperature drop  $\Delta\vartheta$  between in- and outlet is measured by two sets of paired PT 100 thermometers.

### 6. Verification of loss simulation

The verification of the loss simulation methodology is performed in the first step. Measurements are limited to a maximum rotational speed of  $n_{\text{mech}} = 6500$  rpm, a mechanical output torque of  $T_{\text{mech}} = 750$  Nm and a mechanical power of  $P_{\text{mech}} = 200$  kW due to limitations of the used test bench. The measurement is performed at eight different rotational speeds and up to 15 different torque values. The losses are measured for 2 s after the transient response. The machine is thermally conditioned. The temperature is monitored and kept within a range of  $52^\circ\text{C} \pm 2^\circ\text{C}$  for the rotor bar and within  $50^\circ\text{C} \pm 3^\circ\text{C}$  for the stator winding temperature. The comparison of measured power loss  $P_{\text{loss,m}}$  and simulated power loss  $P_{\text{loss,s}}$  is shown in Fig. 6.

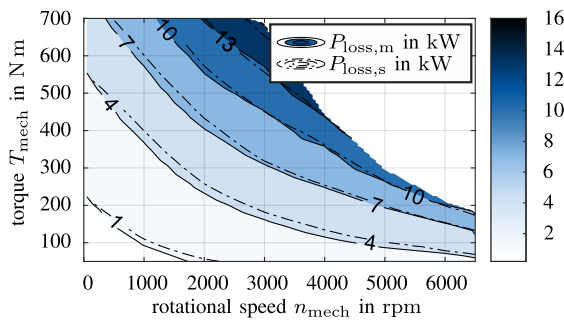


Fig. 6. Verification of loss simulation model: Comparison of losses of simulation  $P_{\text{loss,s}}$  and measurement  $P_{\text{loss,m}}$  in kW

An uncertainty evaluation of the loss measurement is performed according to GUM [17]. The deviations between measurement and simulation are smaller than the expanded uncertainty for all operational points above 200 Nm. The operational points below 200 Nm are in a similar range around 400 W. The simulation model is verified within the uncertainty of the measurement with a level of confidence of  $2\sigma$ .

### 7. Parametrization and study of stator heat paths

Two different measurements are performed for parameterization and study of the heat paths in the stator. The housing cooling is switched on in measurement A, and the winding cooling is used in measurement B. A fluid distribution board is built for switching the cooling circuits. The inlet flow conditions of the cooling circuits are set to a total volume flow rate of  $\dot{V}_{\text{tot}} = 16$  L/min and an inlet temperature of  $\vartheta_{\text{in}} = 25^\circ\text{C}$ . The stator current is increased until maximum temperature of  $95^\circ\text{C}$  is reached in the hottest thermocouple. The stator temperatures  $\vartheta_{s,m}$  are measured for 300 s after the transient response. A maximum temperature change of  $\Delta\vartheta = \pm 1^\circ\text{C}$  is allowed within the measurement time. The rotor cooling circuit is switched on in both measurements to avoid

bearing overheating. Only a minor share of the losses is extracted by the rotor cooling as proved by caloric heat measurements of the cooling circuits in measurement B. The extracted heat by the shaft cooling circuit with  $P_{\text{Shaft}} = 257 \text{ W}$  only makes up  $x = 8.1\%$  of the measured sum of extracted heat by shaft and winding  $P_{\text{Shaft}} + P_{\text{Wind}} = 3164 \text{ W}$ .

The simulation of the 3D-LPTN model shows very good agreement with the measured temperature distribution as shown in Fig. 7, i.e., most of the temperatures have a deviation below  $1^\circ\text{C}$ . The 2D-FEA and the 2D-LPTN also show very good agreement with a majority of deviations below  $1^\circ\text{C}$ . Some locations show higher deviations in both comparisons, e.g., in sensor positions five due to the missing local resolution of the LPTN models. The 3D-LPTN model gives an over-estimation of  $4^\circ\text{C}$  towards measurement, and the 2D-LPTN model gives an over-estimation of  $5^\circ\text{C}$  towards 2D-FEA in location 5. The thermocouple is placed in the corner of the slot. The LPTN models use cuboidal elements that calculate average temperatures of their center and surfaces. They are not capable of predicting the corner temperature accurately. This inaccuracy is acceptable, because the main heat path and the global maximum temperature are predicted accurately.

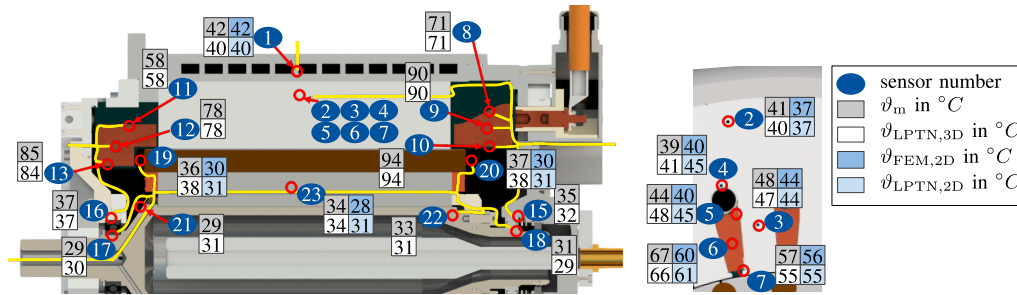


Fig. 7. Temperature distribution in the machine: comparison of measurement, 3D-LPTN, 2D-LPTN and 2D FE-model for measurement B

The models use equivalent interface gaps  $l_{ig}$  to represent the interfaces between the different components in the stator winding slot. The thermal resistance  $R_{ig}$  of the LPTN model of these interface gaps are calculated:

$$R_{ig} = \frac{l_{ig}}{k_{air} \cdot A}, \quad (3)$$

with the thermal conductivity of air  $k_{air} = 0.026 \text{ W/(m K)}$  and the surface area of the interface  $A$ . The interface gaps in the winding slot are parameterized to achieve a good fit between simulation models and measurements. The results of this process are depicted in Fig. 8.

The resulting values vary in a small range between  $0.023 \text{ mm}$  for the interface between insulation and cooling duct and  $0.035 \text{ mm}$  for the interface gap between the surface insulation and the lamination.

The power loss that can be extracted in measurement A with housing cooling is  $P_{\text{loss,m}} = 2620 \text{ W}$  and  $P_{\text{loss,s}} = 2635 \text{ W}$ . The power loss for measurement B is  $P_{\text{loss,m}} = 3276 \text{ W}$  and  $P_{\text{loss,s}} = 3265 \text{ W}$ , respectively. The deviation between measured and calculated losses are below  $1\%$ , i.e., the thermal model can accurately predict the temperature distribution in the winding.

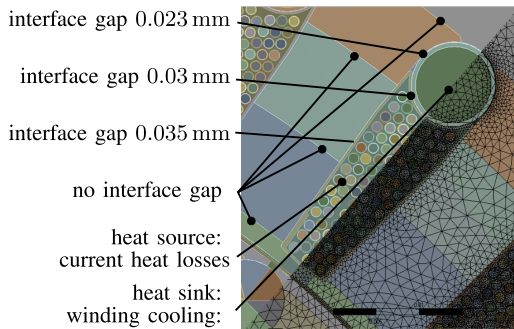


Fig. 8. Result of the parametrization of the interface gaps in the 2D-FEA model

A detailed discussion of the resulting resistances for the winding cooling is performed using the parameterized thermal 2D-FE model. The heat flow density  $\dot{q}$  and the two main heat paths are depicted in Fig. 9. The first heat path goes directly from the stator winding into the stator cooling duct. The second heat path flows out of the stator slot, over the lamination and into the stator cooling duct. The heat  $\dot{Q}_i$  of each path  $i$  that flows across the corresponding area of the cooling duct  $A_i$  is determined

$$\dot{Q}_i = \int_{A_i} \dot{q} dA, \quad (4)$$

with  $\dot{Q}_1 = 606 \text{ W}$  for the direct path and  $\dot{Q}_2 = 1197 \text{ W}$  for the path over the stator lamination. The thermal resistances  $R_{i,j}$  of the components  $j$  along the heat path are studied:

$$R_{i,j} = \frac{\vartheta_{i,j,\text{in}} - \vartheta_{i,j,\text{out}}}{\dot{Q}_i}. \quad (5)$$

The temperature at the in- and outlet  $\vartheta_{i,j,\text{in}}$ ,  $\vartheta_{i,j,\text{out}}$  of each heat path  $i$  and component  $j$  is read from the solution of the finite element analysis. The geometrical location of the paths as

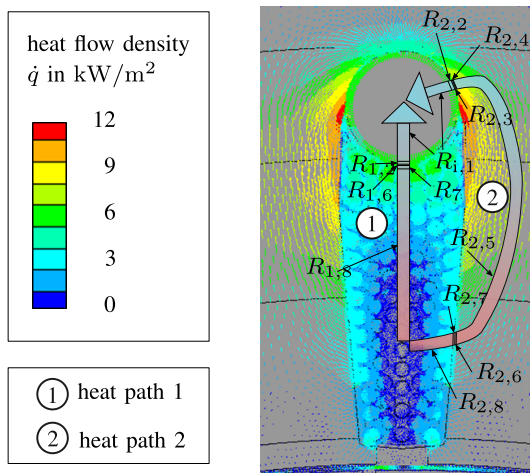


Fig. 9. Detailed study of heats paths and thermal resistances in the stator slot

indicated in Fig. 9 is used for this purpose. Please keep in mind that the temperatures vary over the considered surface, and the calculated resistances depend on the selection of the geometrical temperature evaluation path. The resulting resistances  $R_{i,j}$  are compared in Fig. 10.

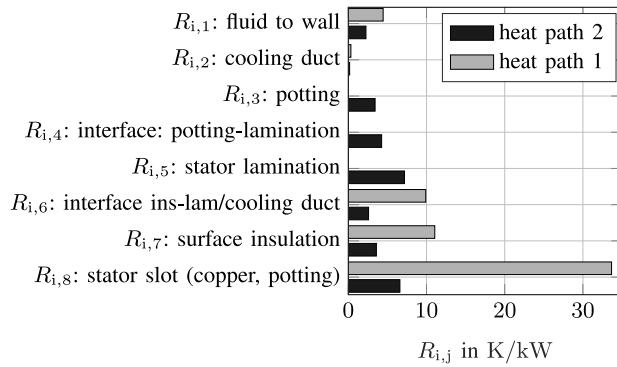


Fig. 10. Comparison of equivalent resistances  $R_{i,j}$  in the slot of the winding cooling

The highest value is calculated for  $R_{1,8} = 33.7$  K/kW that represents the thermal resistance of the copper and insulation inside the slot for heat path 1. It makes up 56% of the resistance of heat path 1 that is the direct path into the stator cooling duct. Resistance  $R_{1,8}$  is the most influential parameter of the cooling design. The thermal resistance over the lamination with  $R_{2,5} = 7.2$  K/kW is significantly lower than  $R_{1,8}$ , but the heat needs to pass some extra resistances for heat path 2. Both heat paths have a low convective thermal resistance between the fluid and the wall  $R_{i,1}$  below 5 K/kW. This low resistance is the result of selecting water-based coolant with good flow conditions and a proper design of the cooling circuit. As discussed later in the study, the volume flow could even be reduced leading to higher resistances  $R_{i,1}$  but to a lower pressure drop of the circuit. The thermal drop across the cooling duct  $R_{i,2}$  is negligible due to the material selection of stainless steel. The thermal interfaces between potting and lamination  $R_{2,4} = 4.3$  K/kW, surface insulation and lamination  $R_{2,6} = 2.6$  K/kW and surface insulation and cooling  $R_{1,6} = 9.9$  K/kW duct have significant impact on the overall thermal resistance of each heat path. A geometrical realignment of the cooling duct in the middle of the slot would thermally improve the design, because  $R_{1,8}$  would be decreased. The mechanical design, the assembly, and the influence on electromagnetic properties would be more complicated in the eyes of the authors. Another possibility of improving the thermal linkage would be a radially aligned thermal conductor in the slot. Alternating eddy currents in such a component need to be avoided. A trade-off between high copper fill factor and good thermal heat extraction is expected. A sensitivity study of the thermal parameters such as introduced in [7] is recommended for future studies.

### 8. Parametrization of rotor heat paths

A similar procedure is performed for the parameterization of the rotor resistances. In this case, the housing cooling is used as a heat source with an inlet temperature of  $\vartheta_{in} = 90^{\circ}\text{C}$ , and the rotor cooling is used as a heat sink with  $\vartheta_{out} = 25^{\circ}\text{C}$ . A measurement time of  $t = 300$  s is used and

a maximum temperature difference of  $\Delta\vartheta = 2^\circ\text{C}$  is allowed within this period. The measurement procedure is repeated for nine different rotational speeds from zero up to  $n_{\text{mech}} = 7000$  rpm. The expanded uncertainty  $U(\dot{Q}_{\text{sh}})$  with a level of confidence of  $2\sigma$  (95.5%) is determined according to GUM [17].

A comparison of measured heat flow  $\dot{Q}_{\text{sh,m}}$  and simulated heat flow  $\dot{Q}_{\text{sh,s}}$  including the uncertainty of the measured heat flow  $U(\dot{Q}_{\text{sh,m}})$  is depicted in Fig. 11.

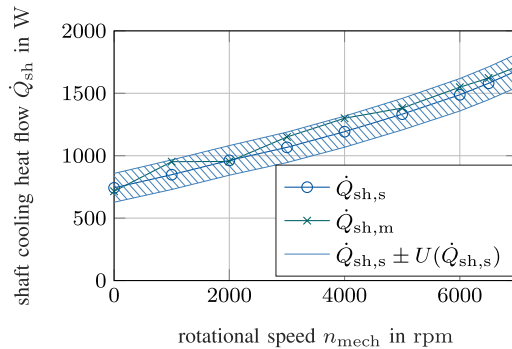


Fig. 11. Comparison of simulation and measurement: heat flow of the shaft cooling  $\dot{Q}_{\text{sh}}$  in W

The simulation  $\dot{Q}_{\text{sh,s}}$  agrees well with the measured values  $\dot{Q}_{\text{sh,m}}$  within the evaluated extended uncertainty of the measurement  $U(\dot{Q}_{\text{sh,m}})$ . The uncertainty with the most significant influence on the overall uncertainty is the maximum temperature difference of the paired thermocouple with 0.1 K. The value becomes relatively more crucial in case less heat is extracted or higher volume flow is selected causing less difference between the temperatures of inlet and outlet. The value of the measured extracted heat increases from 715 W at zero rotational speed up to 1750 W at 7000 rpm. The significant influence is caused by the speed-dependent convective heat transfer phenomena in the machine, e.g., in the air gap, in the end-winding area, or in the shaft cooling.

The temperature of the measurement agrees well with simulation, i.e., the differences are below  $1^\circ\text{C}$  for most of the sensors and below  $3^\circ\text{C}$  for all sensors except for the zero rotational case. This higher deviation is caused by some inaccuracies in the used analytical formula that describe convective effects in the end-winding area. The rotor part of the three-dimensional LPTN model is verified and can be used for the simulation study of different cooling concepts.

## 9. Comparison of cooling concepts

The parameterized electromagnetic and thermal models are used for studying the maximum possible continuous operational power. The maximum allowed temperatures are selected based on the restrictions of the prototype materials, i.e., a maximum winding temperature of  $\vartheta_{\text{wnd,max}} = 180^\circ\text{C}$ , a maximum rotor bar temperature of  $\vartheta_{\text{rb,max}} = 210^\circ\text{C}$ , and a maximum bearing temperature of  $\vartheta_{\text{bear,max}} = 75^\circ\text{C}$ .

An exemplary result of the simulation for model 412 with entire winding cooling and rotor shaft cooling is depicted in Fig. 12. The losses and temperature distribution are calculated in a grid of eleven rotational speeds and up to 22 steps for the torque. The iso-lines for the maximum continuous operational temperatures are added. The line with the lowest torque  $T_{\text{mech}}$  represents

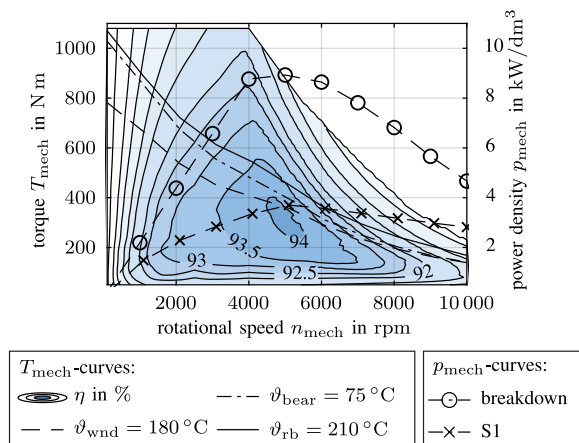


Fig. 12. Operational limits of the simulation model with entire winding and shaft cooling (model 412)

the maximum operational torque without exceeding one of the crucial component temperatures. The power density  $p_{\text{mech}}$  of this line is calculated with the determined mechanical power  $P_{\text{mech}}$ .

$$p_{\text{mech}} = \frac{4 \cdot P_{\text{mech}}}{\pi \cdot d_{\text{ho}}^2 \cdot l_{\text{ho}}} \quad (6)$$

The volumetric power density using the outer diameter  $d_{\text{ho}}$  and the axial length  $l_{\text{ho}}$  of the housing is selected for comparison because installation space is crucial in the studied application. This result of the maximum electrical breakdown torque and the continuous operational torque (S1 according to IEC 60034 1 [1]) is compared in Table 3.

Table 3. Comparison of cooling technologies: characteristic power under continuous operation

Variable	Unit	342	211	311	411	212	312	412
Housing cooling without potting			×			×		
Housing cooling with potting		×		×			×	
Entire winding cooling		×			×			×
No rotor cooling			×	×	×			
Rotor shaft cooling		×				×	×	×
$P_{\text{mech}}$	kW	203	103	82	67	168	175	192
$P_{\text{loss}}$	kW	14.7	7.0	5.9	4.8	13.9	12.5	13.9
$n_{\text{mech}}$	rpm	5 190	5 570	5 060	4 140	5 470	5 310	5 230
$p_{\text{mech}}$	kW/L	3.4	2.0	1.6	1.3	3.2	3.3	3.7
$\vartheta_{\text{max}}$		$\vartheta_{\text{wnd}}$	$\vartheta_{\text{bear}}$	$\vartheta_{\text{bear}}$	$\vartheta_{\text{bear}}$	$\vartheta_{\text{wnd}}$	$\vartheta_{\text{wnd}}$	$\vartheta_{\text{wnd}}$

The influence of the rotor shaft cooling can be studied by comparing the group without rotor shaft cooling (211, 311, 411) with the group with rotor shaft cooling (212, 312, 412). The crucial temperature  $\vartheta_{\text{max}}$  in the first group is the bearing temperature  $\vartheta_{\text{bear}}$ . A crucial heating of the

bearing can be avoided by shaft cooling. The crucial temperature of the three cooling concepts with shaft cooling is the maximum winding temperature  $\vartheta_{\text{wnd}}$ . The three concepts without shaft cooling (211, 311, 411) show power densities between  $p_{\text{mech}} = 1.3 \text{ kW/L}$  for model 411 and  $p_{\text{mech}} = 2.0 \text{ kW/L}$  for model 211. The three concepts with shaft cooling have higher power densities between  $p_{\text{mech}} = 3.2 \text{ kW/L}$  for concept 212 and  $p_{\text{mech}} = 3.7 \text{ kW/L}$  for concept 412. An improvement of the average power density by 108% is possible. This high level of improvement is significantly influenced by the maximum allowable bearing temperature of  $\vartheta_{\text{bear}} = 75^\circ\text{C}$ . Using a high temperature bearing grease with  $\vartheta_{\text{bear}} = 125^\circ\text{C}$  would lead to improved power densities of the groups with the crucial bearing temperature (211, 311, 411) but a significant improvement of 31% in power density would still be possible by using shaft cooling. The stator winding potting increases the power density by 3.1% if housing cooling and shaft cooling are used (312 versus 212). Changing the stator cooling technology from housing cooling with potting to entire winding cooling leads to an increase of the power density of 15.6% (412 versus 212).

The power density of model 311 with housing cooling and potted end-winding with  $p_{\text{mech}} = 1.6 \text{ kW/L}$  is lower than the value of concept 211 with housing cooling without potting, i.e.,  $p_{\text{mech}} = 2.0 \text{ kW/L}$ . A similar behavior can be observed for entire winding cooling with  $p_{\text{mech}} = 1.3 \text{ kW/L}$  for model 411 in comparison to model 211 with housing cooling without potting with  $p_{\text{mech}} = 2.0 \text{ kW/L}$ . This means that the trend of increasing the power density with potting or entire winding cooling cannot be confirmed in case the rotor cooling is switched off. Anyways, the result is coherent with the previous observations and can be explained by the heat paths in the machine. An overview of the heat paths of the built prototype with housing cooling with potting is given in Fig. 13 in a sectional view. The shaft cooling and the entire winding cooling is imaginary switched off for simplification. The shown heat paths are the two main paths to extract current heat losses and iron losses in stator and rotor. The main share is extracted over the active length into the housing cooling. A minor share of the heat is transferred over the end-winding area or the potting to the housing. This second heat path is improved in case full potting is used. The thermal link between end-winding and bearing shield is improved which leads to a temperature increase in the bearing shield. This leads to increased bearing temperatures and a lowered possible power density.

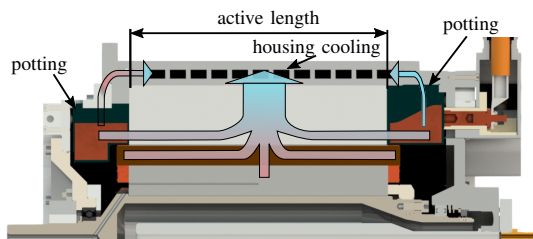


Fig. 13. Heat paths within the machine

## 10. Discussion and future work

The here studied traction machines for heavy-duty application is equipped with three cooling technologies, i.e., entire winding cooling, housing cooling, and shaft cooling. Skin and proximity effects in stator and rotor winding as well as influences of the inverter switching need to be

included in the model to represent the loss behavior of the built prototype. Thermal LPTN and FE models are developed and parameterized using heat path measurements on the machine test bench. The influence of the assembly procedure on interfaces and heat paths is studied. The thermal and loss simulation models agree well with the uncertainty of the used measurement procedure.

The developed models are used to study the influence of different cooling methodologies on the power density of the machine. The maximum permissible bearing temperature is limiting for all models without shaft cooling.

The usage of the shaft cooling leads to a power density improvement of 108% using 75°C bearing grease and to 31% using 125°C bearing grease. The potting of the housing cooling leads to an improvement of 3.1%. The entire winding cooling improves the power density by 15.6%. An incorrect applied improvement of the heat path by potting can lead to a decrease of the power density due to increased bearing temperatures.

Potential for further improvement is identified. The measurement results show significantly higher temperature in the end-winding in comparison to the active length, i.e., temperature at sensor location six in the active length is  $\vartheta_{6,m} = 67^\circ\text{C}$ , and temperature at sensor location 10 in the end-winding is  $\vartheta_{10,m} = 94^\circ\text{C}$  according to measurement B (see Fig. 7). Improved geometry and material of the cooling ducts and the insulation hose in the end-winding could lead to an improved heat extraction from the end-winding.

The introduced cooling concept uses a water-based cooling medium. Using oil-based cooling would lead to higher values of convective resistance  $R_{i,1}$  but comes with advantages of chemical compatibility. A detailed comparison with the suggested water-based design using machine prototypes would be highly appreciated in future work.

The low value of the thermal resistance over the cooling duct  $R_{i,2}$  is preferred on a first glance. A non-conductive cooling duct could simplify the assembly procedure because an additional insulation between the duct and the other machine components would not be necessary. Avoiding such an insulation could improve the values of  $R_{2,3}$  as well as  $R_{2,4}$  and could have an overall positive impact. A study of this trade-off is recommended for future work.

#### Acknowledgements

The here presented work was funded by the Federal Ministry for Economic Affairs and Energy of Germany in the research project “Concept ELV2” (BMW: 01MY17002B).

#### References

- [1] *Rotating electrical machines – Part 1: Rating and performance*, IEC 60034-1:2010, modified (2011).
- [2] Groschup B., Nell M., Hameyer K., *Operational Enhancement of Electric Drives by Advanced Cooling Technologies*, in 2019 IEEE Workshop on Electrical Machines Design, Control and Diagnosis (WEMDCD), Athens, Greece, pp. 65–70 (2019), DOI: [10.1109/WEMDCD.2019.8887761](https://doi.org/10.1109/WEMDCD.2019.8887761).
- [3] Köller S., Uerlich R., Westphal C., Franck M., *Design of an Electric Drive Axle for a Heavy Truck*, ATZ Heavyduty worldwide, vol. 14, no. 2, pp. 20–25 (2021), DOI: [10.1007/s41321-021-0420-8](https://doi.org/10.1007/s41321-021-0420-8).
- [4] Acquaviva A., Skoog S., Thiringer T., *Design and Verification of In-Slot Oil-Cooled Tooth Coil Winding PM Machine for Traction Application*, IEEE Trans. Ind. Electron., vol. 68, no. 5, pp. 3719–3727 (2021), DOI: [10.1109/TIE.2020.2985009](https://doi.org/10.1109/TIE.2020.2985009).

- [5] Camilleri R., Beard P., Howey D.A., McCulloch M.D., *Prediction and Measurement of the Heat Transfer Coefficient in a Direct Oil-Cooled Electrical Machine with Segmented Stator*, IEEE Trans. Ind. Electron., vol. 65, no. 1, pp. 94–102 (2018), DOI: [10.1109/TIE.2017.2714131](https://doi.org/10.1109/TIE.2017.2714131).
- [6] Lindh P., Petrov I., Pyrhonen J., Niemela M., Immonen P., Scherman E., *Direct Liquid Cooling Method Verified with a Permanent-Magnet Traction Motor in a Bus*, in IEEE 8th International Conference on Electrical Machines (ICEM), Alexandroupoli, Greece, pp. 2472–2477 (2018), DOI: [10.1109/TIA.2019.2908801](https://doi.org/10.1109/TIA.2019.2908801).
- [7] Groschup B., Nell M., Pauli F., Hameyer K., *Characteristic Thermal Parameters in Electric Motors: Comparison between Induction- and Permanent Magnet Excited Machine*, IEEE Trans. Energy Convers., vol. 36, no. 3, pp. 2239–2248 (2021), DOI: [10.1109/TEC.2021.3056771](https://doi.org/10.1109/TEC.2021.3056771).
- [8] Staton D., Boglietti A., Cavagnino A., *Solving the More Difficult Aspects of Electric Motor Thermal Analysis in Small and Medium Size Industrial Induction Motors*, IEEE Trans. Energy Convers., vol. 20, no. 3, pp. 620–628 (2005), DOI: [10.1109/TEC.2005.847979](https://doi.org/10.1109/TEC.2005.847979).
- [9] Wrobel R., Mellor P.H., *A General Cuboidal Element for Three-Dimensional Thermal Modelling*, IEEE Transactions on Magnetics, vol. 46, no. 8, pp. 3197–3200 (2010), DOI: [10.1109/TMAG.2010.2043928](https://doi.org/10.1109/TMAG.2010.2043928).
- [10] Groschup B., Rosca A., Leuning N., Hameyer K., *Study of the Thermal Conductivity of Soft Magnetic Materials in Electric Traction Machines*, Energies, vol. 14, no. 17, 5310, pp. 1–18 (2021), DOI: [10.3390/en14175310](https://doi.org/10.3390/en14175310).
- [11] Stephan P., Kabelac S., Kind M., Martin H., Mewes D., Schaber K., *VDI heat atlas*, 2nd ed. Berlin: Springer-Verlag Berlin Heidelberg (2010).
- [12] von Pflingsten G., *The induction machine as speed variable drive for automotive traction applications: Ph.D. dissertation*, IEM of RWTH Aachen University, Herzogenrath: Shaker (2018).
- [13] Kauder T., *Ein Beitrag zum optimalen Entwurf von dreiphasigen Leistungstransformatoren für Mittel-frequenzanwendungen mit höchstmöglicher Ausnutzung und maximal möglichem Wirkungsgrad: Ph.D. dissertation*, IEM of RWTH Aachen University, Aachen: Shaker Verlag GmbH (2021).
- [14] Leuning N., Elfgen S., Groschup B., Bavendiek G., Steentjes S., Hameyer K., *Advanced Soft- and Hard-Magnetic Material Models for the Numerical Simulation of Electrical Machines*, IEEE Trans. Magn., vol. 54, no. 11, pp. 1–8 (2018), DOI: [10.1109/TMAG.2018.2865096](https://doi.org/10.1109/TMAG.2018.2865096).
- [15] *Magnetic materials – Part 3: Methods of measurement of the magnetic properties of electrical steel strip and sheet by means of a single sheet tester*, IEC 60404-3:1992+A1:2002+A2:2009 (2010).
- [16] Bauer D., Mamuschkin P., Reuss H.-C., Nolle E., *Influence of parallel wire placement on the AC copper losses in electrical machines*, in 2015 IEEE International Electric Machines & Drives Conference (IEMDC), Coeur d’Alene, ID, pp. 1247–1253 (2015), DOI: [10.1109/IEMDC.2015.7409221](https://doi.org/10.1109/IEMDC.2015.7409221).
- [17] BIPM, *JCGM 100:2008: GUM 1995 with minor corrections*, Evaluation of measurement data – Guide to the expression of uncertainty in measurement (2008).